DOI: 10.13009/EUCASS2025-643
11TH EUROPEAN CONFERENCE FOR AERONAUTICS AND SPACE SCIENCES (EUCASS)

Development and Testing of a 550 N Additively Manufactured Liquid Rocket Engine Using Green Propellants

Laurence Hoffelder[⋆†], *Ben Oker*[⋆] , *Adrian Matuschik*[⋆], *Felix Klein*[⋆]
[⋆]*Hybrid Engine Development - HyEnD e.V., Student Group of the University of Stuttgart*
Pfaffenwaldring 29, 70569 Stuttgart
laurence.hoffelder@hyend.de
[†]Corresponding author

Abstract

HyEnD, a student rocketry group from the University of Stuttgart, is developing a regeneratively cooled liquid rocket engine through the BLAST project, aiming to break the altitude record for student-built liquid rockets. The engine utilizes nitrous oxide as oxidizer and ethanol as fuel. It also incorporates regenerative cooling for extended burn times and reusability. Additive manufacturing enables the creation of complex cooling channel geometries that would be impractical or cost-prohibitive when using conventional manufacturing methods. Furthermore, additive manufacturing allows for rapid prototyping and short lead times which is crucial for a student led research project. The development process of the 550 N demonstrator engine started with ignition testing using an ablatively cooled battleship engine to characterize ignition behavior and establish a reliable ignition sequence. The regenerative cooling design proceeded in two phases: First, determining initial cooling parameters and channel dimensions through a simplified custom model, followed by detailed computational fluid dynamics (CFD) simulation for optimization.[6] The final engine design was manufactured using Laser Metal Fusion (LMF) technology. Utilizing 3D computer tomographic scans, the geometrical accuracy of the additively manufactured engine with its integral cooling channels was examined and the effectiveness of different powder removal procedures were analyzed. Finally the engine underwent testing on a purpose-built test stand. The measurements were compared with design tool predictions to enhance future modeling capabilities.

1. Introduction

Traditionally, space propulsion systems have relied on toxic propellants such as hydrazine or dinitrogen tetroxide. In an effort to reduce the environmental impact of space travel, current research increasingly focuses on non-toxic alternatives, commonly referred to as green propellants. The shift towards green propellants in satellite propulsion is also relevant to student rocketry, where low toxicity and ease of availability are paramount. In both contexts, propulsion systems utilizing nitrous oxide as an oxidizer are particularly appealing.[16]

HyEnD, a student group at the University of Stuttgart, has a notable history of employing nitrous oxide in hybrid rockets. Their HEROS 3 rocket, launched in 2016, set an altitude record for student hybrid rockets.[9,10] This record was nearly doubled to 64 km in 2023 by HyEnD's N2ORTH rocket.[8] Following the N2ORTH campaign, the BLAST project was initiated, which now aims to develop a bi-liquid rocket. For this system, ethanol was selected as the fuel in combination with nitrous oxide due to its favorable performance characteristics and availability. To enable reusability, the rocket engine will incorporate regenerative cooling. However, manufacturing combustion chambers with integrated cooling channels using conventional methods is both complex and costly.[16] Therefore, additive manufacturing is employed in the production of the combustion chambers.

Currently, propulsion systems combining nitrous oxide and ethanol remain uncommon, with publicly available research primarily limited to studies by Tokudome et al.[17] and Youngblood et al.[19] This paper aims to contribute to the existing body of research by presenting the design and testing of a 550 N sub-scale, additively manufactured combustion chamber using nitrous oxide and ethanol as propellants.

First, a comprehensive overview of the fundamental equations governing heat transfer, injector design and overall performance estimation is provided. Based on these principles, the subsequent section outlines the design methodology. This is followed by a detailed description of the additive manufacturing process, including procedures for powder removal. Finally, the experimental setup, test execution and results are discussed.

DOI: 10.13009/EUCASS2025-643

2. Governing Equations

This section gives an overview of the basic equations applied in this work. For more details the reader is referred to the reference literature.[13, 16]

2.1 Equations of Heat Transfer

To calculate the heat transfer coefficient $\alpha_{\text{chamberWall}}$ on the hot gas side, the Nusselt correlation by Cinjarew is proposed by Schmidt.[15] For the channel heat transfer coefficient $\alpha_{\text{channelWall}}$ the Nusselt correlation by Kraussold was used. These are calculated as following:

Cinjarew

$$Nu_{\text{Cinjarew}} = 0,0162\,(RePr)^{0,82}\left(\frac{T_{\text{stag}}}{T_{\text{chamberWall}}}\right)^{0,35}, \tag{1}$$

where T_{stag} is the stagnation temperature and $T_{\text{chamberWall}}$ is the combustion chamber temperature. The best matching with experimental data is reached for the thermophysical properties at the temperature: $T = (T_{\text{rec}} + T_{\text{chamberWall}})/2$ according to Schmidt.[15] To obtain this temperature, the so called recovery temperature T_{rec} has to be calculated first with the stagnation temperature T_{stag}, the recovery factor r_{c}, the adiabatic combustion temperature T_{comb} as well as the combustion efficiency η_{comb}:

$$T_{\text{rec}} = T_{\text{stag}} r_{\text{c}}\left(T_{\text{comb}}\eta^2_{\text{comb}} - T_{\text{stag}}\right). \tag{2}$$

Kraussold

$$Nu_{\text{Kraussold}} = 0,024Re^{0,8}Pr^{0,37}\left(1 + \frac{D_{\text{h}}}{x}\right)\left(1 + 1,75\frac{D_{\text{h}}}{r}\right), \tag{3}$$

where x and r are the local length and radius respectively, while D_{h} is the hydraulic diameter of the channel.

Heat conduction Conduction can be described with the following formula whereas $\dot{Q}$ ist the heat flux, d the thickness of the wall, A the penetrated wall area, λ the thermal conductivity, r the radius, L the element length, α the heat transfer coefficient and R the heat resistance:

$$\dot{Q} = \frac{T_1 - T_2}{R_\lambda} \tag{4}$$

$$\dot{Q} = \dot{m}\,(T_{\text{out}} - T_{\text{in}}) = \dot{m}\left(c_{\text{p,out}}T_{\text{out}} - c_{\text{p,in}}T_{\text{in}}\right) \tag{5}$$

$$R_\lambda = \frac{d}{\lambda A} \tag{6}$$

$$R_\lambda = \frac{1}{2\pi L\lambda}\ln\left(\frac{r_2}{r_1}\right) \tag{7}$$

$$R_\alpha = \frac{1}{\alpha A} \tag{8}$$

For heat transfer mechanisms the resistance is described with the help of the heat transfer coefficient calculated from the Nusselt number:

$$Nu_{\text{D}_\text{h}} = \frac{\alpha D_{\text{h}}}{\lambda_{\text{Fluid}}}. \tag{9}$$

For the Nusselt correlation the so called hydraulic diameter D_{h} is needed. It is calculated with the cross-sectional area A and its circumference U:

$$D_{\text{h}} = 4\frac{A}{U}. \tag{10}$$

The Prandtl number Pr and the Reynolds number Re needed for various flow calculations are calculated as following:

$$Pr = \frac{c_{\text{p}}\eta}{\lambda}, \tag{11}$$

$$Re_{\text{D}_\text{h}} = \frac{v_\infty \rho}{\eta}D_{\text{h}}. \tag{12}$$

The recovery factor r_c from Eq.2 is estimated using the Prandtl number:

$$r_{\text{c}} \approx \sqrt[3]{Pr}. \tag{13}$$

DOI: 10.13009/EUCASS2025-643

2.2 Rocket Performance

To evaluate the performance of a rocket engine, measurable properties like propellant mass flow rates, thrust and chamber pressures are normalized to allow for the comparison of propellant combinations and different propulsion systems.

$$I_{\mathrm{sp}} = \frac{F_{\mathrm{T}}}{\dot{m} \cdot g_0} = \frac{\dot{m} \cdot u_{\mathrm{e}} + (p_{\mathrm{e}} - p_{\mathrm{a}}) \cdot A_{\mathrm{e}}}{\dot{m} \cdot g_0}. \tag{14}$$

The weight specific impulse I_{sp} is obtained through normalizing the thrust with the combustion gas mass flow rate and the gravitational constant. The specific impulse of a rocket engine is proportional to the characteristic velocity c^* of the propellant combination, which describes the thermochemical merit of a propellant combination to achieve high exhaust velocities.[13,16] As real rocket engine performance is non-ideal, the characteristic velocity efficiency $\eta_{c^*} = \frac{c^*_{\mathrm{exp}}}{c^*_{\mathrm{id}}}$ can be defined as the ratio between the experimentally determined characteristic velocity and the ideal achievable characteristic velocity. The experimentally determined characteristic velocity is defined as

$$c^*_{\mathrm{exp}} = \frac{p_{\mathrm{t0,exp}} \cdot A_{\mathrm{th}}}{\dot{m}_{\mathrm{exp}}}, \tag{15}$$

where $p_{\mathrm{t0,exp}}$ is the total chamber pressure, A_{th} is the throat area and $\dot{m}_{\mathrm{exp}}$ the combustion gas mass flow. The ideal performance parameters for a given engine configuration, operating chamber pressure, propellant combination and operating mixture ratio $OF = \frac{\dot{m}_{\mathrm{ox}}}{\dot{m}_{\mathrm{f}}}$ are obtained through chemical equilibrium calculations using the application NASA Chemical Equilibrium with Applications (CEA).[4] Analyzing η_{c^*} of experimental rocket engine tests allows for the comparison of combustion performance of different engine configurations, combustion chamber geometries and injector designs.[13,16]

2.3 Equations for Injector Sizing

The injector of a liquid rocket combustion chamber is tasked with atomizing the propellants during their injection into the combustion chamber and influences the droplet formation, vaporization speed, mixing of propellants, combustion efficiency, combustion stability and wall heat flux.[18] There are different types of rocket propellant injectors with different geometric and operative characteristics. The simplest injector type is a so-called shower head injector, consisting of small axial holes in the injector plates, that use high flow speeds of the propellants to create small droplets of propellant. Impinging jet injectors have 2 or more angled holes through which propellant jets flow and collide at an impingement point creating fine droplet sheets. Centrifugal swirl injectors use special swirl chamber geometries with tangential holes to create a helical flow pattern within the swirl chamber with high tangential velocity forming thin sheets of propellant upon exiting the swirl chambers into the combustion chamber. This leads to fine atomization of the propellants.

The analytical design process of a rocket engine injector revolves around the discharge coefficient of the injectors describing the ratio of real mass flow to ideal mass flow passing through the injectors combined orifice area. In general, the propellant mass flow rate $\dot{m}_{\mathrm{Prop}}$ through the injector can be calculated according to[2,18]

$$\dot{m}_{\mathrm{Prop}} = C_{\mathrm{d}} A_{\mathrm{inj}} \sqrt{2 \rho_{\mathrm{Prop}} \Delta p_{\mathrm{inj}}}, \tag{16}$$

where C_{d} is the discharge coefficient, A_{inj} is the critical area of the injector, ρ_{Prop} is the density of the fluid and Δp_{inj} is the pressure drop over the injector.

Different empirical correlations and analytical design procedures exist for calculating C_{d} for different types of injectors. These will be discussed in a later section. After obtaining the discharge coefficient, the injector is sized for a target pressure drop of 20-25 % of the chamber pressure as a suitable value to allow for adequate decoupling of combustion chamber and the feed system to avoid feed system coupling instabilities.[18]

DOI: 10.13009/EUCASS2025-643

3. Engine Design Process

This chapter details the design methodologies and considerations for the main subsystems of the rocket engine.

3.1 Ignition System Design

Three ignitor types were considered within this work: COTS pyrotechnic signal ammunition, solid model rocket motors (Klima D9-P), and steel wool (Ballistol 0000). All ignitors were initiated with an e-Match. Signal ammunition and steel wool were positioned within the combustion chamber. The model rocket motor, due to its size, was placed with its nozzle exit in the diverging section of the main engine, directed inward. Ignition test results are detailed in section 5.2.1.

3.2 Injector Design

The choice of injector depends on the chosen propellant combination, oxidizer to fuel ratios, state of matter of the propellants at injection, geometric parameters of the combustion chamber as well as additional factors like manufacturability. In the development process of the liquid combustion chamber, a significant effort was put on developing and testing the injectors due to their major influence on overall engine performance.

Impinging jet injectors were selected for the demonstrator combustion chamber as these injectors promise good atomization of propellants, repeatable droplet sheet formation, comparatively simple geometries of injection holes and distribution manifolds. Impinging jet injectors can be classified by the number of injection jets impinging at a single impingement point and by the type of propellant impinging. Two jets of oxidizer impinging on a single point would be classified as a Like-on-Like doublet impinging jet injector. The number of impinging jets can vary from 2 up to 4-5 influencing the atomization and geometry of the droplet sheet. However, at higher numbers of impinging jets the droplets start to agglomerate into larger droplets reducing the atomization effectiveness of the injector. For the case that oxidizer and fuel impinge at a single impingement point the classification would be described as Like-on-Unlike impingement.[18]

The design of impinging jet injectors followed an iterative design algorithm described by Bazarov.[18] The discharge coefficient of the impinging jet injectors is iteratively calculated using pressure loss coefficients due to wall friction within the injection holes, inflow losses and constrictor losses dependent on the geometric parameters of individual injector holes. The algorithm adjusts the hole diameter, calculates the Reynolds number in the injector holes and converges on a final discharge coefficient. Using this algorithm, the impinging jet injector holes were sized for both ethanol and nitrous oxide utilizing the physical properties at the expected injection pressure and injection temperature dynamically provided by the fluid property database CoolProp.[3, 11]

The injection angle of the impinging jet injectors influences the atomization and droplet sheet formation significantly. However, manufacturability, manifold placement and hole pattern are also relevant design parameters for impinging jet injector design. The resulting momentum balance of a planar doublet impinging jet element consisting of 2 jets impinging in a single point is relevant for evaluating the resulting flow direction of the droplets and the formation and size of possible recirculation zones within the combustion chamber. The resulting spray angle θ of two impinging jets can be calculated from the momentum balance according to:[16]

$$\tan\theta = \frac{m_1 u_1 \sin\gamma_1 - m_2 u_2 \sin\gamma_2}{m_1 u_1 \cos\gamma_1 - m_2 u_2 \cos\gamma_2}, \tag{17}$$

where m_1, m_2 are the massflow rates of the individual jets, u_1, u_2 are the jet velocities and γ_1, γ_2 are the jet angles.

Two different types of impinging jet injectors were developed and tested within the demonstrator combustion chamber. Additionally coaxial swirl injectors were also developed and will be investigated in future tests.

3.2.1 Like-Like Nitrous Oxide Doublet + Ethanol Like-Like Triplet Injector

A Like-on-Like impinging jet injector having 6 doublet impingement elements of nitrous oxide positioned in a concentric ring and a single central triplet impingement element for the ethanol. For the nitrous oxide doublets an opening angle of 90° was chosen and the resulting droplet sheet angle is 15° towards the central axis of the combustion chamber. In the center of the injector three ethanol jets impinge in a triplet single element injector. The inward angle of the nitrous oxide droplet sheet results in a secondary impingement point of oxidizer droplets and fuel droplets after roughly 0.3 times the chamber length.

DOI: 10.13009/EUCASS2025-643

3.2.2 Like-Like-Unlike Triplet Injector

The second type of impinging jet injector consists of 9 Like-Like-Unlike triplet elements positioned on a concentric ring, where 2 nitrous oxide jets and a single ethanol jet impinge at a single impingement point. The already tested injector is shown in figure 1 and 2 The resulting momentum balance of the 3 jets still has a 8° droplet sheet angle towards the central axis of the combustion chamber resulting in a secondary impingement point at 0.4 times the chamber length. As ethanol and nitrous oxide droplets already mix in the impingement action, combustion reactions can start closer to the injector plate and therefore have a longer effective combustion chamber length to complete the reaction. Consequently, this injector design promises higher combustion efficiencies.

3.2.3 Coaxial Swirl Injectors

The investigation into suitable injectors for the demonstrator combustion chamber also included the preliminary design and manufacturing of different types of swirl injectors. The design process of the coaxial swirl injectors followed the theory discussed in.[18] Multiple different coaxial swirl injectors with both ethanol and nitrous oxide internal and external swirl chambers as well as recessed internal swirl chambers have been designed and manufactured, one example is shown in figure 3. Both conventional and additive manufacturing were utilized in the production process of these swirl injectors. The in-depth testing of these injectors is the focus of one of the upcoming test campaigns and ignitability, combustion stability and combustion efficiency will be evaluated accordingly.

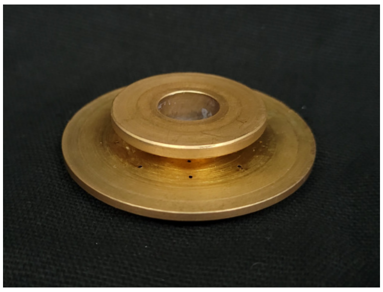

Figure 1: Like-Like-Unlike Triplet impingement viewed from the injector manifold side

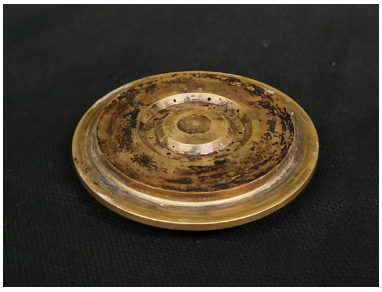

Figure 2: Like-Like-Unlike Triplet impingement viewed from the combustion chamber side

Figure 3: Coaxial swirl injector assembly. Left: Inner swirl chamber; Right: Outer swirl chamber

3.3 Cooling System Design

This chapter deals with the cooling system design routine that was used to determine a sufficient cooling channel design.

3.3.1 MATLAB Cooling Channel Analysis Tool

To make an estimation concerning the temperature profile at the chamber and channel walls as well as the cooling fluid, a 2D MATLAB Tool was developed. This tool solves the thermal equilibrium at distinct positions along the chamber contour. It uses several simplifications:

- No axial heat transport
- No radiation
- Homogeneous fluid temperature profile across cross sections
- 1D flow
- No flow losses
- Trapezoidal cross section
- Homogeneous heat flux below cooling channel
- Adiabatic outside wall

To calculate the temperature profile, the MATLAB tool uses cells along the engine contour as follows:

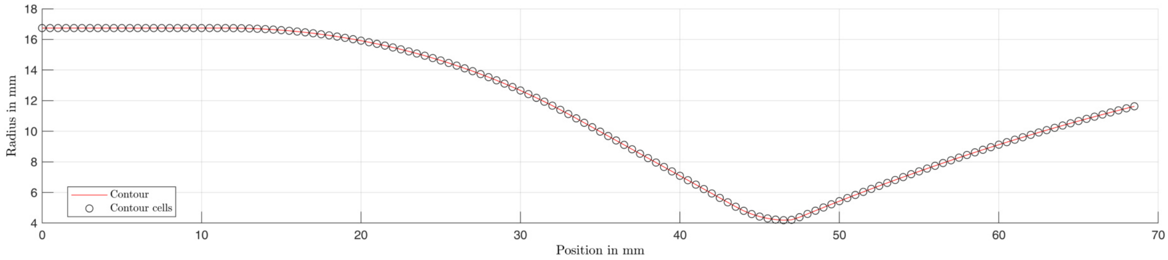

Figure 4: Contour cells

Discretization Each cell covers a length **dx** along the contour. Thus the whole engine is divided into $n = \frac{L}{dx}$ cells, for each of which an average state across the cell is determined. In order to determine the temperature profile for the cells, the adiabatic flow characteristic along the chamber is calculated first. This is later needed to calculate the heat transfer coefficient $\alpha_{\text{chamberWall}}$ on the hot gas side.
The contour cells themselves are built up as a pie slice, meaning only one cooling channel and the wall segment covered by it are calculated. They are built up as shown in figure 5.

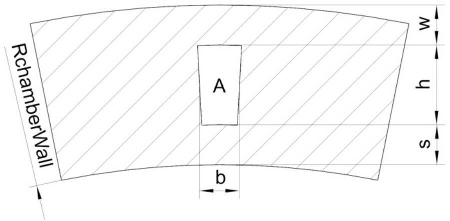

Figure 5: Cooling channel cross section

Table 1: Cooling channel parameter

A	area of cross section
b	width
h	height
s	distance to the chamber wall
w	distance to outer wall
$R_{\text{chamberWall}}$	chamber wall radius

Heat flux The the equations for the stationary heat flux is put together from the following wall heat fluxes.

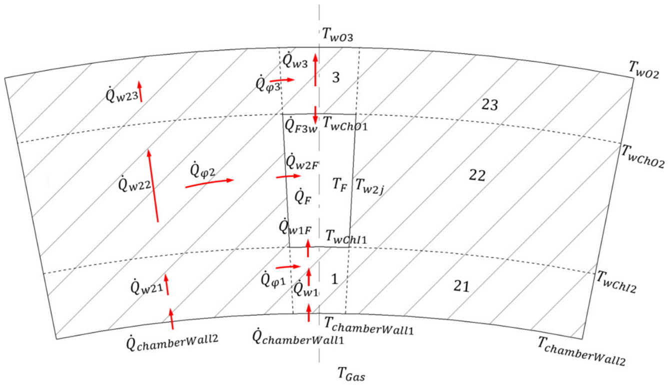

Figure 6: Wall heat fluxes

To calculate the radial heat fluxes, an average temperature for the wall field is used. This can be calculated as following:

$$T_{\text{av}} = \frac{\int_{r_1}^{r_2} T(r)\,dr}{r_2 - r_1} = \frac{\left(\ln\left(\frac{r_2}{r_1}\right) T_1 + T_1 - T_2\right) r_1 - \left(\ln\left(\frac{r_2}{r_1}\right) T_2 + T_1 - T_2\right) r_2}{\ln\left(\frac{r_2}{r_1}\right)(r_1 - r_2)}. \tag{18}$$

The analytical calculation of the average temperature as described above, although very precise, results in high program run times in a complex solving algorithm for the temperature field as shown in fig.6. Therefore, a linear segmenting approach to calculate the average was chosen. In this approach the median temperature is added in segments whereas each is an increase in radius by the length **dx**. This temperature is then divided by the number of steps. This results in a resolution of "$n = (r_2 - r_1)/dx$" with a average temperature of:

$$T_{\text{av}} = \sum_{i=1}^{\frac{r_2-r_1}{dx}} T_{\text{m}} + T_1 + \left(\frac{T_2 - T_1}{\ln\left(\frac{r_2}{r_1}\right)} \ln\left(\frac{r_1 + dx\,(r_2 - r_1)}{r_1} \right) \right). \tag{19}$$

Heat fluxes are only considered as shown in fig.6. Axial heat fluxes between the contour cells as seen in fig.4 are not considered. This results in a calculated maximum temperature higher than the real occurring temperature which is considered acceptable as it provides a greater safety margin against destruction of the chamber wall.

3.3.2 CFD Analysis

Following the analytical dimensioning with use of the MATLAB tool further analysis via Computational Fluid Dynamics (CFD) was conducted. Therefore, the application Fluent by ANSYS was used.[1]
In order to keep calculation times down a RANS approach was chosen.[5, 14] For turbulence modeling a k-ω-SST model was selected as for heat transfer problems the wall interactions are of importance. For heat transport problems at the wall a dimensionless wall distance y^+ of ≤ 1 must be chosen.[12]

Table 2: CFD boundary conditions

CFD boundary conditions:			
Combustion temperature	T_0	K	3228
Chamber outlet pressure	p_{chamberE}	Pa	101325
Chamber massflow	$\dot{m}_{\text{chamberCFD}}$	$\text{kg}\,\text{s}^{-1}$	$\dot{m}/n_{\text{ch}}$
Cooling channel inlet temperature	T_{f0}	K	300
Cooling channel outlet pressure	p_{chE}	MPa	8
Cooling channel massflow	$\dot{m}_{\text{chCFD}}$	$\text{kg}\,\text{s}^{-1}$	$\dot{m}_{\text{ch}}/n_{\text{ch}}$
Sand equivalent roughness	k_{s}	mm	0,5

Table 3: Combustion gas properties

Combustion gas properties:			
Positions of the engine	Chamber	Throat	Exit
Temperature in K	2412	2184	1087
C_{p} in $\text{kJ}\,\text{kg}^{-1}\,\text{K}^{-1}$	1.800	1.665	1.346
Viscosity in $1 \times 10^{-5}\cdot\text{Pa}\,\text{s}$	8.454	7.910	5.002
Conductivity in $\text{W}\,\text{m}^{-1}\,\text{K}^{-1}$	0.2377	0.1991	0.09817

The boundary conditions and combustion gas, according to the NASA CEA application,[4] for the CFD Simulation can be extracted from table 2 and table 3. The simulation converges for various cooling channel geometry variations for a characteristic mesh size of $\sim 8 \times 10^{-5}$ mm.

4. Manufacturing Process

This chapter describes the manufacturing process of the combustion chamber, with a particular focus on the application of additive manufacturing techniques.

4.1 Additive Manufacturing of the Combustion Chamber

Laser powder bed fusion (LPBF) is a powder based additive manufacturing process, where fine metal powder is selectively melted using a laser beam. The machine applies thin layers of fresh powder and repeats the laser process layer by layer until a finished additively manufactured part is completed. Through this method, the complex internal cooling channel geometries can be printed in place.

Understanding the LPBF process is a key aspect for the optimization of the part design for this manufacturing process. While immense geometrical freedom is given, this manufacturing process also comes with its own limitations.

DOI: 10.13009/EUCASS2025-643

Printing large overhangs is difficult as the melt pool can sink into the powder bed upon solidification, creating a depression in the new layer. Maximum unsupported overhang angles of up to 50° are common. Through support material, larger overhang angles are printable but require tedious removal process of these metal support structures. Therefore, the 316L test bench version of the 550 N combustion chamber features a conical upper section avoiding the need to print with supports.

For the cooling channel design in the internal combustion chamber walls, the minimum printable wall thickness is an important design parameter. The wall thickness between cooling channels in the throat area of the combustion chamber limits the maximum number of cooling channels of a given thickness. Furthermore the minimum wall thickness between the cooling channel and internal combustion chamber wall greatly influence the wall heat flux, wall temperature and therefore the overall cooling channel effectiveness. Incorporating the limitations of the used machines and materials, a minimum wall thickness of 0.5 mm between the cooling channel and internal combustion chamber wall and 0.4 mm between two cooling channels was chosen.

4.2 Post-Processing after LPBF

After the printing of a combustion chamber different post processing steps are required to get to the final part. The first step after removing the printed part from the build plate is depowdering and removal of the support structures.

Then the important sealing surfaces of the part are machined using conventional subtractive machining. Internal stresses created by the printing process can cause warping in the part during machining. Figure 10 shows the machining of the different fluid adapter ports, where both the thread and the gasket sealing surface for the high pressure oxidizer need to be machined. Additionally, mating surfaces with relevant tolerances are post processed. All machined surfaces are printed slightly oversized so that the conventional machining process can bring the parts into the tolerance window.

4.3 Computer Tomography of the Combustion Chamber

While the external geometry of the combustion chamber can be inspected easily, the important geometry like cooling channels and distribution manifolds sit within the combustion chamber wall. To analyze the internal geometry, the combustion chamber was scanned using a computer tomography, where multiple 2D detector images, as shown in image 7, are taken using x-rays, that can later be reconstructed in a 3D model of the actual printed part. This was done on a Zeiss Metrotom 800 320kV machine.

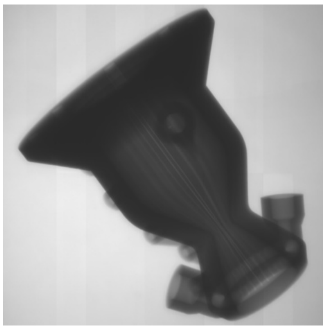

Figure 7: CT scan detector image of 316L engine

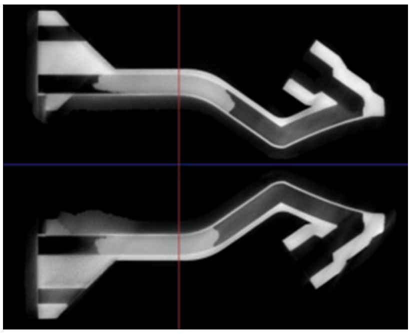

Figure 8: CT section view through clogged internal cooling channel

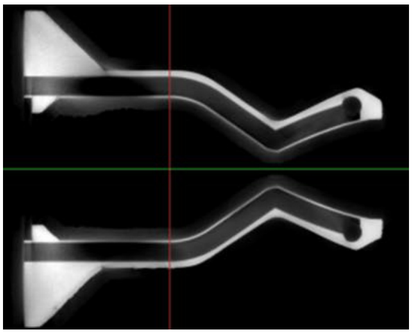

Figure 9: CT section view through unclogged internal cooling channel

The scan results of the 550N combustion chamber revealed great geometrical soundness of the print. The analysis of the real wall thickness revealed only a deviation of 0.05 mm of the target wall thickness of 0.5 mm, which is remarkably accurate for this printing technology. An immediate scan result revealed clogged cooling channels as shown in figure 8. This blocks coolant flow through the channels compromising cooling performance. As conventional depowdering methods applied immediately after the printing process did not solve this issue, a high pressure water depowdering method was applied. This is detailed in section 4.4.

4.4 High Pressure Water Depowdering

To remove the compacted and stuck powder in some of the cooling channels, a high pressure water flushing was conducted. For this process a dedicated flange and seal was designed, that enables all but one cooling channel to be

DOI: 10.13009/EUCASS2025-643

blocked at the same time. This allows for the entire water pressure to force itself through a single cooling channel and out the single slot of the flange that is visible in figure 11 and 12.

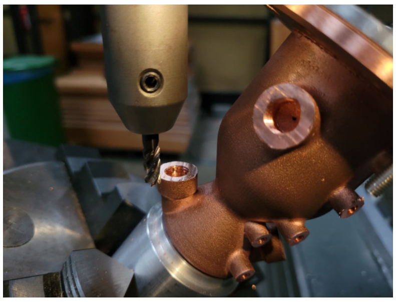

Figure 10: machining of sealing surface for manifold N2O connectors

Figure 11: depowdering flange with slot for single cooling channel

Figure 12: depowdering setup mounted to the rocket engine

This depowdering method successfully cleared the clogged cooling channels. The pressure drop to ambient pressure during the flushing process of every cooling channel was monitored through a pressure sensor and compared. By ensuring an equal pressure drop across every individual cooling channel it was certain, that the previously clogged cooling channels were freed up. The resulting freed up cooling channels can be seen in figure 9.

5. Engine Testing

This chapter details the experimental campaign conducted to validate the design and performance of the designed engine.

5.1 Test Bench Setup

HyEnD has built and is operating a test bench for bi-liquid engine tests of up to 600 N. This small scale test bench is built on a mobile frame and can be moved using a small wagon to our testing location at a certified explosives bunker at the University of Stuttgart.

5.1.1 Hydraulics and Thrust Measurement

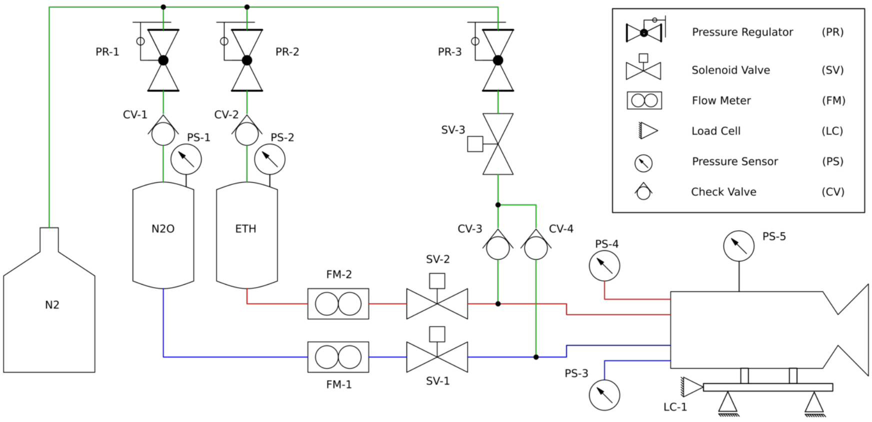

Figure 13: HyEnD mobile liquid rocket engine test bench fluid plan

Two separate intermediate tanks are filled with the propellants ethanol and nitrous oxide as shown in the test bench fluid plan in figure 13. Each intermediate tank is isolated from the pressurization system through check valves (CV-1, CV-2) and has their own pressure regulator (PR-1, PR-2) to allow for independent pressurization of oxidizer and fuel to operate the same injector and combustion chamber at different OF-ratios. The pressurization system is supplied with 200 bar nitrogen gas from a nitrogen bottle. Two solenoid main valves (SV-1, SV-2) are positioned in front of the liquid engine actuated independently to allow for different ignition timings. To measure the mass flow rate of the

DOI: 10.13009/EUCASS2025-643

propellants, two coriolis sensors (FM-1, FM-2) are positioned after the runtanks. A third pressure regulator (PR-3) is used for the nitrogen purge line at 10 bar purging pressure with a third solenoid purging valve (SV-3) attached to the main oxidizer and fuel lines right after the main valves to clear out excess propellants from the feed line and extinguish and cool the engine after a hotfire test. The engine itself is mounted on a thrust structure consisting of a linear rail that allows axial movement. A load cell (LC-1) is positioned at the end of the linear rail and pretensioned through springs. This allows for axial thrust measurements and the pretension eliminates the influence of the static friction in the linear rail.

5.1.2 Sensors and Electronics

The testbench is controlled through a National Instruments USB-6501 data acquisition unit running LabView software reading analog sensor data and controlling the valve timing and ignitor signal through the digital output channels. Two pressure sensors monitor the tank pressure in the fuel and oxidizer run tanks, two pressure sensors measure the injection pressure of the propellants right in front of the injector while another pressure sensor attached to the combustion chamber measures the chamber pressure for efficiency and performance evaluations. WIKA A10 pressure sensors with a measuring range of 0-200 bar are used with an ensured maximum error of ±0.05 %. The measurement frequency is set to 250 Hz. The thrust of the engine is measured through a Kistler 9351B 0-10 V piezo electric force sensor. The measured preload of the spring pretensioning mechanism is removed within the measurement software. The measurement frequency of the load cell is 250 Hz. The coriolis mass flow sensors are measuring both the density and the mass flow of the propellants at a frequency of 50 Hz. The nitrous oxide coriolis sensor is a TCM 5500 and the ethanol coriolis sensor a TCM 650.

5.2 Battleship Engine Test Results

Rocket engine testing involves inherent risks, particularly from hard starts, ignition failures and detonations. A conservative approach was adopted by performing initial tests with a battleship combustion chamber featuring ablative cooling and simplified geometry. This battleship test engine can be manufactured using only conventional machining techniques and allows for easy internal chamber geometry modifications.[7] Such geometric freedom combined with a damage-tolerant design facilitates less expensive and rapid testing, enabling fast design iterations.

5.2.1 Ignition Testing

The initial testing campaign aimed to evaluate various ignition methods, as detailed in Section 3.1, and to establish a reliable ignition sequence for the engine. The first series of runs utilized steel wool ignited by an e-Match. However, in ignition tests, the steel wool consistently failed to ignite the engine. This was attributed either to immediate extinguishing by an ethanol fuel lead or to expulsion from the engine during an oxidizer lead sequence. Consequently, this ignition method was not pursued further. Greater success was observed with the use of a solid motor for ignition. The solid motor's nozzle exit was positioned in the diverging section of the battleship engine via a 3D-printed mount. This configuration successfully ignited the engine. However, these tests revealed significant ignition overpressures, reaching values approximately twice the engine's operational pressure. The first successful test was followed by two "hard starts," which resulted in the forward flange being blown off due to the excessive overpressure, terminating the tests. It is hypothesized that this hard-starting behavior stemmed from the substantial distance between the ignitor flame and the injector, allowing an ignitable mixture to accumulate in the combustion chamber before ignition. As the solid motor's size precluded its placement directly inside the chamber this ignition method was also discontinued. An oxidizer lead was not investigated in this configuration. The signal ammunition proved to be the most successful ignition method. Given that signal ammunition burns fuel-rich, an oxidizer lead was chosen. This sequence allowed the oxidizer to react with the ignitor, filling the combustion chamber with hot gas prior to fuel injection. In monopropellant tests (oxidizer only ignition), this method produced a significant chamber pressure indicating successful combustion of the oxidizer with the signal ammunition. For bipropellant operation, an initial fuel delay of 0.5 s was selected, which resulted in successful ignition with only a minor ignition overpressure, as shown in figure 14. Through successive tests, the fuel delay was reduced to 0.2 s. A challenge encountered was the accumulation of tough metallic residues from some signal ammunition compositions, which plugged small holes in the ethanol injector before the fuel valve opened. To mitigate this issue, the signal ammunition was switched to a different, non-metallic composition that does not produce solid residues. This setup proved to be the most reliable ignition method and was consistently employed in subsequent tests.

5.2.2 Injector Characterization

To evaluate the performance of the different injectors, multiple hotfire tests with different chamber and injector configurations were conducted. Figure 14 shows the injection and chamber pressure of the like-like-unlike impingement injector test while figure 15 shows the thrust and propellant mass flow measurements during the tests. The chamber pressure data indicates steady-state operation of the liquid rocket engine after an ignition transient of ≈ 0.3 s. The valve timing and oxidizer lead of 0.2 s is also visible in the mass flow rate measurements shown in figure 15. In this test the average chamber pressure of 46.5 bar was below the target operating point due to lower than expected mass flow rate of the oxidizer. Consequently, the average OF-ratio of 3.1 was slightly fuel rich and the achieved thrust was below the target thrust. Statistical average values of the measured pressures, thrust and mass flow rates were utilized and the discharge coefficient of the oxidizer and fuel injectors was calculated according to equation 16 while the I_{sp} and c^* were calculated according to equation 14 and 15.

	p_{cc} in bar	OF-ratio	$C_{\text{d,ox}}$	$C_{\text{d,fuel}}$	η_{c^*}	I_{sp} in s
Like-Like	43.7 ±0.1	3.1 ±0.08	0.442	0.722	0.883 ±0.011	-
Like-Like-Unlike	46.5 ±0.1	3.03 ±0.08	0.427	0.749	0.958 ±0.011	218 ±3.4

Table 4: average test results of different impingement injector tests

Table 4 summarizes the test results and calculated performance parameters of the like-like-unlike and like-like impingement injector tests. Due to an error in the thrust measurement of the like-like-impingement injector test, no I_{sp} could be computed. Both tests were below target chamber pressure and target OF-ratio and therefore represent comparable operating points. The discharge coefficient evaluation of both injectors reveals good agreement between the tests, while the discharge coefficient of the nitrous oxide injector holes is significantly lower than the ethanol injector holes. Comparing the c^*-efficiency of both tests, a significant improvement of $\approx 7.4\%$ can be observed by using the like-like-unlike injector over the like-like injector.

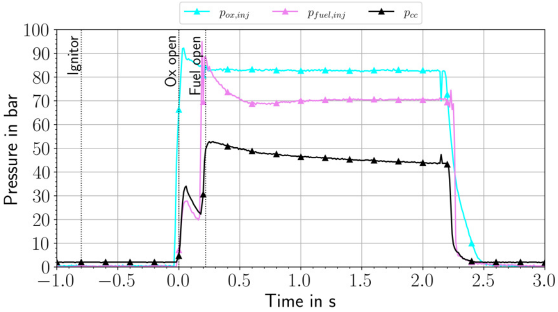

Figure 14: injection- and chamber pressure of like-like-unlike impingement injector test

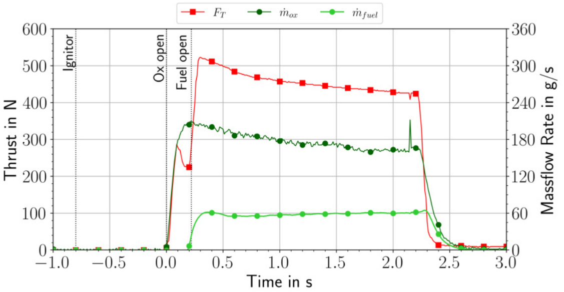

Figure 15: thrust and propellant mass flow rates of like-like-unlike impingement injector test

This improved c^*-efficiency indicates higher combustion gas temperature and combustion completeness. Comparing the exhaust plumes of both engine tests, the plume of the like-like injector test shown in figure 16 is glowing in a bright orange color coming from the emission spectrum of unburnt carbon atoms and carbon monoxide radicals reacting with atmospheric oxygen. In comparison, the exhaust plume of the like-like-unlike injector tests glows in a pale blue color due to the absence of unburnt carbon, which confirms the higher combustion efficiency and completeness caused by this injector. These results conclude an overall better performance of the like-like-unlike impingement injector. Furthermore, additional improvements on injector hole geometry have to be made to hit design operating chamber pressure and OF-ratio in future tests.

Figure 16: like-like-unlike impingement injector test

Figure 17: like-like-unlike impingement injector test

DOI: 10.13009/EUCASS2025-643

5.3 AM Combustion Chamber Testing

To evaluate the cooling channel design routine and choice of material, hotfire tests were conducted. For these tests an OF-ratio of 8 was targeted to reduce the combustion temperature for a conservative approach. The thermodynamic and transport properties have been determined with the NASA CEA[4] application. The parameters are described in tab. 3. The first design of cooling channels has been made for a combustion chamber from 316L with successive designs for alternative wall materials with different thermophysical properties to improve combustion chamber performance.

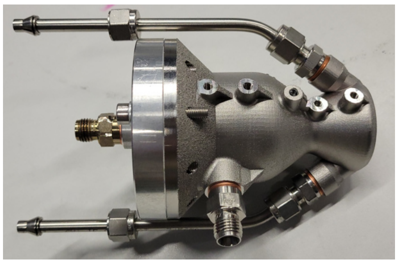

Figure 18: 316L engine with plumbing

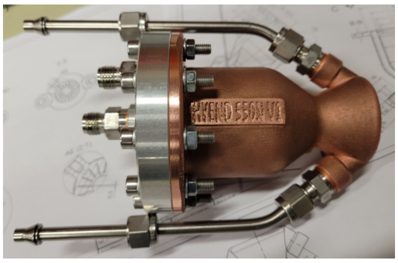

Figure 19: copper engine with plumbing

Figure 20: copper engine mounted on the test bench

5.3.1 Hotfire Test of 316L Combustion Chamber

For the 316L combustion chamber, a preliminary cooling channel geometry was determined using a MATLAB tool. This yielded an optimally printable design consisting of 32 channels, each with a width of 0.5 mm, a height of 5 mm, and a wall spacing of 0.5 mm. The maximum wall temperature predicted by the MATLAB tool is 867.7 K. These characteristic temperatures were subsequently verified using an ANSYS k-ω SST simulation in Fluent.[1] The ANSYS CFD simulation provides an area-weighted average outlet temperature of 366.5 K for the cooling channels. At the throat, the wall temperature is 1026.5 K according to the CFD results. Although the simulation predicts localized wall temperature peaks upstream of x = 2.5 mm, these are considered negligible due to inlet effects from the sharp entry angle, which result from simplifications in the CFD model.

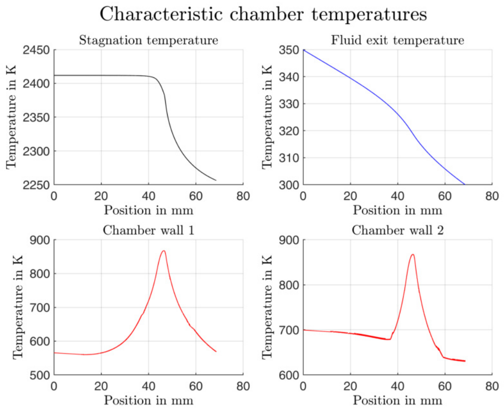

Figure 21: MATLAB output temperatures: 316L Engine

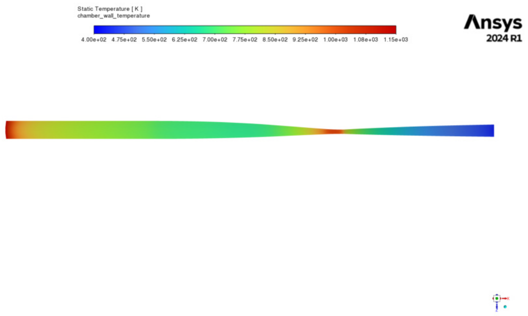

Figure 22: CFD chamber wall temperature

The MATLAB tool indicates that the steel operates within acceptable temperature limits, whereas the CFD results predict excessively high throat temperatures for operation in this configuration. To validate and calibrate the simulation tools, a hot-fire test of the 3D-printed engine was conducted, as shown in fig.23.

In fig.24, a drop in manifold temperature can be observed immediately after the nitrous oxide valve opens, due to throttling effects. The heat absorbed by the cooling channels is insufficient to maintain a constant nitrous oxide temperature. A near-steady combustion phase is evident once the ignitor is fully consumed, at approximately 1.1 s. However, the measured temperatures continue to rise thereafter. It should be noted that the pressure port of the combustion chamber was partially obstructed, allowing only qualitative assessment of chamber pressurization, with no reliable quantitative data.

DOI: 10.13009/EUCASS2025-643

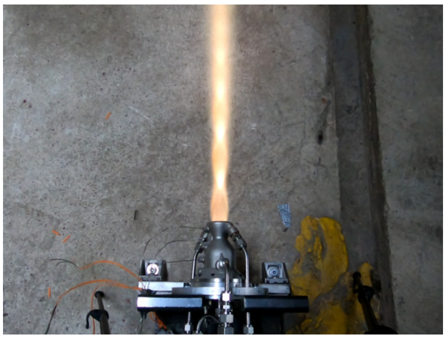

Figure 23: Hotfire Test: 316L Engine

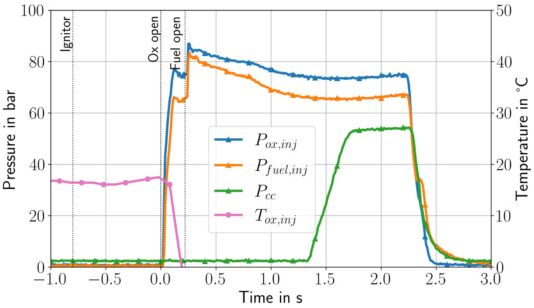

Figure 24: Hotfire Test: 316L Engine Data

Following the test, a CT scan of the engine was conducted to assess the condition of the chamber wall. Due to the narrow spacing of the cooling channels, thermocouples had to be positioned above them, preventing accurate wall temperature measurements or analysis. The scan revealed significant erosion of the wall material in the throat region, with burn-through into the cooling channels. This damaged area closely corresponds to the region of maximum thermal load predicted by the CFD simulation and MATLAB tool.

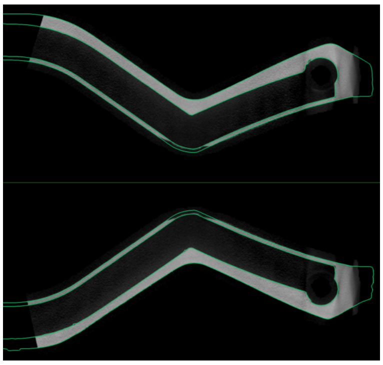

Figure 25: CT scan section through the side of tested engine. Green lines are the initial contour before testing

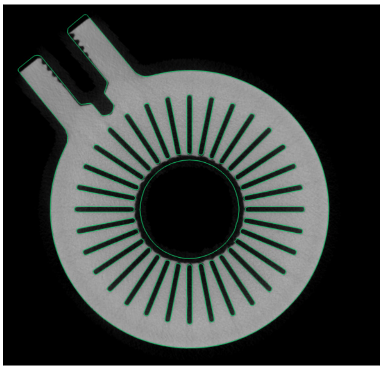

Figure 26: CT scan section at the throat of the tested engine. Green lines are the initial contour before testing

5.3.2 Hotfire Test of Copper Combustion Chamber

To investigate materials with high thermal conductivity, CuCr1Zr was initially selected, as this alloy promises good performance for a scaled-up 1.6 kN engine. However, CuCr1Zr was unavailable from our supplier, so pure copper was used for the first engine with high-conductivity chamber walls. The use of nitrous oxide as a coolant at 80 bar places it in the supercritical regime inside the injector manifold. Since nitrous oxide is a relatively potent solvent, the decision was made to assess potential solvent effects of supercritical nitrous oxide on seals in this demonstrator engine, provided that sufficient heat can be transferred into the fluid. Therefore, a cooling channel geometry was determined using the MATLAB tool, consisting of a height of 5 mm, width of 0.5 mm, a wall spacing of 0.5 mm, and a total of 16 channels. This configuration yields a fluid exit temperature of 355.2 K, which lies within the supercritical regime.

The hot-fire test data, as shown in fig.28, confirms this assumption. In contrast to the steel combustion chamber, the oxidizer pre-injector temperature which corresponds to the cooling channel exit temperature begins to rise once ignition occurs. Upon nitrous oxide injection, the temperature increases immediately as combustion initiates between the fuel-rich ignitor plume and the nitrous oxide. The critical point of nitrous oxide is at 36.4 °C and 72.4 bar.[11] This critical point is exceeded at approximately 0.3 s, at which point the injector manifold is filled with supercritical nitrous oxide. At around 0.4 s, a rapid pressure drop can be observed in the data from fig. 28. This event corresponds to a rapid unscheduled disassembly of the engine beyond the injector flange. The cause was determined to be the dissolution of the sealant by the supercritical nitrous oxide in the manifold, which subsequently enabled combustion upstream of the injector.

DOI: 10.13009/EUCASS2025-643

Additionally, it should be noted that the port for the combustion chamber pressure sensor was either fully or partially clogged during the test, resulting in unusable data. The available data only confirms that pressure built up in the combustion chamber, thereby indicating that combustion occurred.

Figure 27: Hotfire Test: Copper Engine Data

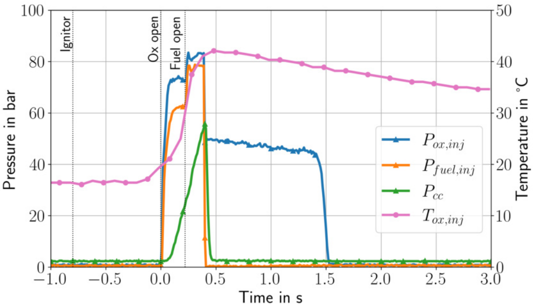

Figure 28: Hotfire Test: Copper Engine

6. Conclusion and Future Work

This paper detailed the development and initial testing of a 550 N liquid rocket engine utilizing green propellants. A key aspect of this project was the integration of additive manufacturing techniques, which proved instrumental in fabricating complex cooling channel geometries that would be impractical with conventional manufacturing methods. The design of the regenerative cooling system followed a two-phase approach, beginning with a simplified custom model for initial parameter determination, followed by detailed CFD simulations for optimization. The engine was then manufactured using LBPF methods. The integrity of the manufactured engine, particularly its internal cooling channels, was verified using 3D computer tomographic scans. This advanced inspection method was crucial in identifying manufacturing defects such as clogged channels. To address the clogging issues, a high-pressure water depowdering method was applied. Initial ignition testing on an ablatively cooled battleship engine established a reliable ignition sequence using signal ammunition with a 0.2 s fuel delay, demonstrating successful ignition with only minor overpressures. After a successful ignition sequence was found, testing efforts were directed to the regeneratively cooled engine, where combustion chambers made from 316L and copper were tested. The 316L chamber experienced significant burn-through while the copper engine test failed due to the nitrous oxide becoming supercritical and bypassing the seals in the injector head. As a consequence, we changed our sealants from polymer-based seals to graphite-based sealants. Future work will focus on several key areas to advance the development of this liquid rocket engine. A primary objective is to validate simulation results concerning cooling channel heat transfer through experimental verification. This will involve comprehensive testing of different materials, including Inconel 718, 316L, and copper, as well as an investigation into the performance of various cooling channel geometries. Additionally, further efforts will be directed towards the testing and development of advanced injector designs, particularly coaxial swirl injectors, and the creation of specialized injectors optimized for supercritical nitrous oxide. Looking ahead, the project aims to scale up the engine's thrust, with plans to develop an engine with over 8 kN of thrust.

7. Acknowledgments

We would like to thank the Materialprüfanstalt (MPA), the Institute of Space Systems (IRS) and our sponsors for their support of the BLAST project. We would also like to express our special thanks for the support provided by the Baden-Württemberg Ministry of Science, Research and Arts within the framework of the „Zukunftsoffensive Luft- und Raumfahrt“.

DOI: 10.13009/EUCASS2025-643

References

[1] Ansys Inc. *ANSYS FLUENT 12.0 Theory Guide*, 2009.

[2] V. Bazarov, V. Yang, and P. Puri. Design and dynamics of jet and swirl injectors. *Liquid Thrust Chambers: Aspects of Modeling, Analysis and Design*, 200(19-103), 2004.

[3] Ian H. Bell, Jorrit Wronski, Sylvain Quoilin, and Vincent Lemort. Pure and pseudo-pure fluid thermophysical property evaluation and the open-source thermophysical property library coolprop. *Industrial and Engineering Chemistry Research*, 53(6):2498–2508, 2014.

[4] Sanford Gordon and Bonnie J McBride. Computer program for calculation of complex chemical equilibrium compositions and applications. part 1: Analysis. Technical report, 1994.

[5] Jan Haemisch. *Wärmeübergang von Wasserstoff und Methan in Kühlkanälen regenerativ gekühlter Schubkammern kryogener Raketentriebwerke*. Phd-thesis, r Fakultät fÃ¼r Maschinenwesen, Rheinisch-Westfälischen Technischen Hochschule Aachen, 2024.

[6] Laurence Hoffelder. Cfd-kühlkanaloptimierung eines regenerativ gekühlten n2o-ethanol triebwerks. In *Institutsseminarreihe DLR Lampoldshausen*, 2024.

[7] T Kahn and I Qamar. Factors affecting characteristic length of the combustion chamber of liquid propellant rocket engines. *Mehran University Research Journal of Engineering and Technology*, 38(3), 2019.

[8] Indira Keserovic, Colin Barth, Julian Dobusch, Marc Gritzka, Marc Hazenbiler, Philipp Jochum, Florian Merz, Robert Rödinger, and Maximilian Oechsle. Design and launch of the hybrid sounding rocket n2orth. In *26th ESA Symposium on European Rocket and Balloon Programmes and Related Research*, 05 2024.

[9] Mario Kobald, Ulrich Fischer, Konstantin Tomilin, Anna Petrarolo, Paula Kysela, Christian Schmierer, Andreas Pahler, Jonas Gauger, Jonas Breitinger, Ferdinand Hertel, and Benjamin Hochheimer. Sounding rocket "heros" - a low-cost hybrid rocket technology demonstrator. 07 2017.

[10] Mario Kobald, Christian Schmierer, U. Fischer, Konstantin Tomilin, and Anna Petrarolo. A record flight of the hybrid sounding rocket heros 3. In *31st International Symposium on Space Technology and Science (ISTS)*, 06 2017.

[11] E. W. Lemmon, I. H. Bell, M. L. Huber, and M. O. McLinden. NIST Standard Reference Database 23: Reference Fluid Thermodynamic and Transport Properties-REFPROP, Version 10.0, National Institute of Standards and Technology, 2018.

[12] C.K. Mangrulkar, J.D. Abraham, and A.S. Dhoble. Numerical studies on the near wall y+ effect on heat and flow characteristics of the cross flow tube bank. *Journal of Physics*, 1240(1), 2019.

[13] D Mishra. *Fundamentals of Rocket Propulsion*. CRC Press, 2017.

[14] Ferry Roelofs. *Thermal Hydraulics Aspects of Liquid Metal Cooled Nuclear Reactors*. 2019.

[15] Günther Schmidt. *Technik der Flüssigkeits-Raketentriebwerke*. 1999.

[16] G. Sutton and O. Biblarz. *Rocket Propulsion Elements*. Wiley, 9 edition, 2017.

[17] Shinichiro Tokudome, Tsuyoshi Yagishita, Ken Goto, Naohiro Suzuki, Takayuki Yamamoto, and Yasuhiro Daimoh. An experimental study of an n_2o / ethanol propulsion system with 2 kn thrust class bbm. *Transactions of the Japan Society for Aeronautical and Space Sciences, Aerospace Technology Japan*, 19(2):186–192, 2021.

[18] V. Yang, M. Habiballah, J. Hulka, and M. Popp. *Liquid Rocket Thrust Chambers: Aspects of Modelling, Analysis and Design*. American Institute of Aeronautics and Astronautics, 2004.

[19] Stewart H. Youngblood. Design and testing of a liquid nitrous oxide and ethanol fueled rocket engine. Master's thesis, New Mexico Institute of Mining and Technology, Socorro, New Mexico, August 2015.